Title
Spatial statistics for detecting mechanical interactions among fiber fractures

Journal
Journal of the Mechanics and Physics of Solids, 216

ISSN
0022-5096

Authors
Gallagher, Shane P
Zok, Frank W

Publication Date
2026-10-01

DOI
10.1016/j.jmps.2026.106783

J. Mech. Phys. Solids 216 (2026) 106783

Contents lists available at ScienceDirect

Journal of the Mechanics and Physics of Solids

journal homepage: www.elsevier.com/locate/jmps

Spatial statistics for detecting mechanical interactions among fiber fractures

Shane P. Gallagher, Frank W. Zok *

Materials Department, University of California, Santa Barbara

ARTICLE INFO

Keywords:
Composites
spatial statistics
fiber fracture
load sharing
point process
anisotropy
pair correlation function

ABSTRACT

Inferring mechanical interactions from the spatial organization of discrete damage events is a fundamental inverse problem in the mechanics of heterogeneous materials. This work develops a statistical framework for extracting load-transfer interactions from three-dimensional fiber fracture data in unidirectional fiber-reinforced composites. Conventional micromechanical models typically assume global load sharing (GLS), implying statistically independent fiber fracture events, whereas growing experimental evidence suggests that load redistribution can become localized, producing spatially autocorrelated fracture. To distinguish these effects, classical second-order spatial statistics are extended by decomposing pairwise separations into transverse and axial components, reflecting the directional asymmetry of stress redistribution in fiber composites. Analytical solutions are derived for two canonical GLS models that establish a mechanics-based null hypothesis for mechanical independence. Unlike conventional approaches based on complete spatial randomness, this null hypothesis explicitly accounts for both the underlying fiber arrangement and the observed axial break intensity profile, allowing arbitrary fracture distributions to be analyzed without assuming a particular axial form. A normalized fiber interaction statistic is then introduced to remove these contributions, enabling direct assessment of mechanically induced coupling between neighboring fibers and meaningful comparison among datasets with different fiber arrangements and break distributions. Monte Carlo simulations quantify estimator variability and demonstrate that localized interactions can be detected with high statistical power even when only a modest fraction of fiber breaks are mechanically coupled. The resulting framework provides a rigorous methodology for interpreting volumetric fracture data and establishes a quantitative bridge between experimentally observed spatial damage patterns and micromechanical load-sharing models. Although demonstrated for fiber fracture in unidirectional composites, the underlying methodology is broadly applicable to heterogeneous materials in which damage evolves through discrete spatial events.

1. Introduction

Understanding how local mechanical interactions give rise to spatially organized damage is a central problem in the mechanics of heterogeneous materials. Advances in experimental characterization now make it possible to reconstruct the three-dimensional locations of discrete damage events—including cracks, voids, particle fractures, and fiber breaks—with unprecedented fidelity. These

* Corresponding author.
E-mail address: zok@ucsb.edu (F.W. Zok).

https://doi.org/10.1016/j.jmps.2026.106783
Received 16 May 2026; Received in revised form 13 July 2026; Accepted 17 July 2026
Available online 18 July 2026

datasets contain, in principle, the statistical signature of the underlying interaction mechanisms responsible for damage evolution. The central challenge, however, is to distinguish spatial organization arising from genuine mechanical interactions from patterns produced solely by specimen geometry, heterogeneous distribution of potential damage sites, or statistical fluctuations. Addressing this inverse problem is essential if volumetric damage datasets are to be used to infer the governing mechanisms of material failure.

Fiber-reinforced composites provide a particularly compelling model system for this problem. When a fiber breaks, load is redistributed both axially along the broken fiber and transversely to neighboring fibers through the surrounding matrix (Thouless and Evans, 1988; Sutcu, 1989; Curtin, 1991a; Hui et al., 1995). The nature of this redistribution determines whether damage evolves diffusely or localizes into clusters, ultimately controlling composite strength and toughness. In the broader context of heterogeneous materials, these composites provide a rigorous testbed for developing methodologies capable of inferring load-transfer mechanisms directly from experimentally observed damage patterns.

Models of composite tensile response typically assume global load sharing (GLS). In this idealized limit (Hui et al., 1995), the load shed by a broken fiber is redistributed uniformly among all intact fibers, implying statistically independent fracture events. However, substantial experimental evidence suggests that local load sharing (LLS) plays an important role in real composites. Evidence includes statistically correlated fiber pullout lengths (Han et al., n.d.), large acoustic emission events consistent with simultaneous fiber failure (Swaminathan et al., 2021), coplanar fiber breaks observed in tomographic datasets (Swolfs et al., 2015), and measured composite strengths that fall below predictions of GLS-based models (Morscher, 1997; Rossoll et al., 2012; Almansour et al., 2015; Han et al., 2025). Together, these observations suggest that fiber breaks produce localized stress concentrations that elevate the probability of subsequent failures in neighboring fibers, leading to spatially correlated fracture and premature composite failure.

Finite element studies have sought to quantify local load transfer and its influence on damage progression and composite fracture (Ibnabdeljalil and Curtin, 1997; Landis and McMeeking, 1999; Landis et al., 2000). While these simulations have provided valuable mechanistic insight, they generally rely on constitutive and interfacial parameters that are difficult to determine experimentally and are often computationally intensive. More importantly, translating predicted interaction mechanisms into experimentally measurable statistical signatures has remained largely unexplored. Consequently, a rigorous methodology for inferring load-sharing behavior directly from experimental observations has yet to emerge.

Existing approaches for analyzing fiber fracture data largely treat fracture locations as descriptive observations rather than quantitative evidence of the underlying mechanics. Previous work demonstrated that spatial statistics can extract useful information from fiber fracture patterns measured on composite fracture surfaces using confocal microscopy to determine fracture heights and in-plane spatial coordinates (Han and Zok, 2026; Han et al., n.d.). Statistical measures such as Geary's C, semivariograms, and pair correlation functions were shown to provide useful descriptors of fracture organization. However, because fiber fracture height was treated as a continuous scalar field defined over the transverse plane, the analysis was fundamentally restricted to two-dimensional measurements and to fiber breaks exposed on the final fracture surface.

The rapid development of high-resolution X-ray computed tomography (XCT) fundamentally changes this problem. Rather than providing isolated observations of fracture surfaces, XCT enables reconstruction of the complete three-dimensional distribution of fiber breaks within a composite at multiple stages of loading, offering a much richer basis for statistical analysis (Swolfs et al., 2015; Badran et al., 2020; Hilmas et al., 2020). These volumetric datasets contain, in principle, the full statistical signature of the underlying load-transfer mechanisms. The challenge is no longer acquiring the data but extracting mechanics from it in a statistically rigorous and physically meaningful manner.

Spatial point process theory provides a natural framework for addressing this inverse problem because it treats discrete damage events as realizations of an underlying stochastic process. Point process theory has been applied across a wide range of disciplines, including ecology (Cizungu et al., 2021), astronomy (Hurtado-Gil et al., 2021), biology (da Silva et al., 2008), materials science, (Terban and Billinge, 2022), and composite materials (Chateau et al., 2015; Bhattacharyya and Adams, 2021).

The simplest descriptors of a spatial point process are first-order statistics, which characterize spatial intensity—the expected number of points per unit length, area, or volume (Ripley, 1977, 2005; Diggle, 1983). In the present context, the first-order statistic corresponds to fiber break intensity, which varies along the specimen length owing to the presence of matrix cracks (Sutcu, 1989; Callaway and Zok, 2020; Hilmas et al., 2020). Although these measures describe where fracture events occur, they cannot distinguish between statistically independent and mechanically correlated fracture. That distinction requires second-order statistics.

Second-order statistics quantify pairwise point structure through the distribution of interpoint separations. These are analogous to covariance in classical statistics: they describe not only how many events occur, but how those events are organized relative to one another. In spatial statistics, quantities such as Ripley's K function and the pair correlation function (PCF) measure clustering or inhibition in the pairwise point structure relative to an appropriate reference process (Ripley, 1977, 2005; Diggle, 1983). From a mechanics perspective, first-order statistics characterize the local density of damage events, whereas second-order statistics quantify the spatial organization arising from interactions among those events. These statistics therefore provide a means of quantifying how local stress redistribution influences the probability of subsequent fracture events.

A principal limitation of conventional second-order spatial statistics is that they implicitly assume isotropic interactions (Ripley, 1977, 2005; Diggle, 1983). This assumption is fundamentally incompatible with the mechanics of fiber-reinforced composites. Stress redistribution is highly directional: axial load recovery occurs along the broken fiber through shear lag, whereas transverse load transfer is mediated through the surrounding matrix. The characteristic interaction distances differ substantially, reflecting distinct physical mechanisms. Consequently, isotropic statistics conflate fundamentally different interaction processes and can obscure the statistical signatures of local load transfer.

The objective of the present work is to develop a mechanics-based statistical framework for inferring load-transfer interactions from three-dimensional spatial damage data. Although motivated by fiber fracture in unidirectional composites, the methodology addresses the broader inverse problem of inferring interaction mechanisms from the spatial organization of discrete damage events. By decomposing pairwise separation distances into transverse and axial components, we derive anisotropic extensions of Ripley's K function and the pair correlation function that explicitly reflect the directional mechanics of stress redistribution. Anisotropic extensions of second-order spatial statistics are themselves well established and have previously been applied to point patterns with similar columnar structure (Møller et al., 2016; Safavimanesh and Redenbach, 2016). The present contribution is to place these statistics within a mechanics-based framework that enables mechanical interactions to be inferred directly from spatial fracture patterns. Under global load sharing, the resulting statistics reduce to separable analytical forms, establishing a rigorous null hypothesis for mechanical independence between fibers.

To facilitate inference from experimental datasets, we introduce a normalized *fiber interaction statistic*, Ψ, that removes the confounding influences of fiber arrangement and nonuniform axial break intensity, thereby isolating the statistical signature of mechanically induced interactions. Analytical solutions are derived for two canonical global load-sharing models—the single fiber composite (SFC) and single matrix crack (SMC)—providing exact reference states for interpreting experimental observations. Monte Carlo simulations are then used to quantify estimator variability and evaluate the statistical power of the proposed framework for detecting localized load sharing, even when only a modest fraction of fracture events are mechanically coupled. More broadly, the methodology provides a mechanics-based framework for interpreting volumetric damage datasets and distinguishing mechanically induced spatial organization from that arising solely from specimen geometry and nonuniform event density.

The remainder of the paper is organized as follows. Section 2 introduces the relevant concepts and notation from spatial statistics. Section 3 presents analytical expressions for second-order fiber break statistics under the SFC and SMC global load-sharing models. Section 4 examines the variability of the proposed estimators for finite datasets using Monte Carlo simulations. Section 5 evaluates the statistical power of these measures for detecting departures from global load sharing. Finally, the implications of the framework are discussed in Section 6, followed by concluding remarks in Section 7.

Table 1
List of symbols and abbreviations.

d	Spatial dimension	PCF	Pair correlation function
e_{ij}	Edge correction for points i and j	PDF	Probability density function
f	Fiber volume fraction	$P_{\Delta Z}$	Cumulative probability of pairwise break axial separation distances
$g(r)$	Isotropic PCF	$\mathbb{R}^d$	d-dimensional space
$g_b(r_\parallel)$	Fiber break PCF (axial)	R_f	Fiber radius
$g_b(r_\perp, r_\parallel)$	Fiber break PCF (3D)	$SD[\cdot]$	Standard deviation
$g_f(r_\perp)$	Fiber PCF	SFC	Single fiber composite
g_{NN}	Nearest-neighbor PCF statistic	SMC	Single matrix crack
$\bar{l}_b$	Average break spacing	U	Uniform distribution
$\bar{l}_p$	Average distance between breaks and matrix crack plane	Z	Axial position (random variable)
m	Fiber Weibull modulus	α	Nominal false positive rate
n	Number of neighboring points	δ_f	Fiber slip length
n_b	Number of neighboring breaks	δ_m	Matrix slip length
n_f	Number of neighboring fibers	$\Delta r_\parallel$	Axial bin width
p_t	Triggered-break fraction	$\Delta r_\perp$	Transverse bin width
p_Z	PDF of break axial positions	ΔZ	Axial separation distance (random variable)
$p_{\Delta Z}$	PDF of pairwise break axial separation distances	ε	Applied strain
r	Isotropic separation distance	λ	Intensity
$r_\parallel$	Axial separation distance	λ_b	Fiber break intensity
$r_\perp$	Transverse separation distance	λ_f	Fiber intensity
s	Dummy integration variable	σ_f^*	Characteristic fiber stress
z	Axial position	σ_f^0	Weibull reference stress
CSR	Complete spatial randomness	σ_p	Peak fiber stress (at matrix crack plane)
D	Spatial observation region	τ_s	Interface sliding stress
E_f	Fiber Young's modulus	$\Psi(r_\perp, r_\parallel)$	Fiber interaction statistic
$\mathbb{E}[\cdot]$	Expected value	Ψ_{NN}	Nearest-neighbor interaction statistic
GLS	Global load sharing	$1(\cdot)$	Indicator function
$K(r)$	Isotropic Ripley's K	$(\cdot)^+$	Positive-part operator
$K_b(r_\parallel)$	Fiber break Ripley's K (axial)		
$K_b(r_\perp, r_\parallel)$	Fiber break Ripley's K (3D)		
L	Composite gauge length		
L_0	Weibull reference length		
N	Total number of points		
N_b	Total number of fiber breaks		
N_f	Total number of fibers		

2. Point Processes and Spatial Statistics

2.1. Preliminaries

A point process is a random countable set of points in a finite domain in d-dimensional space. The intensity of the process, λ, is the expected number of points per unit length, area, or volume. A process is *homogeneous* if its intensity is constant throughout the domain and *stationary* if its statistical properties are invariant under translation; stationarity therefore implies homogeneity, though the converse does not necessarily hold. The process is *isotropic* if its properties are invariant under rotation.

Spatial point processes fall into two broad classes: Poisson-type processes, in which points are independent and noninteracting, and Gibbs-type processes, in which points interact. The canonical Poisson-type process is the homogeneous Poisson process, which serves as the baseline model of complete spatial randomness (CSR): intensity is constant, point counts in any region D follow a Poisson distribution with mean $\lambda|D|$, and counts in disjoint regions are independent (Ripley, 1977, 2005). A subclass of Gibbs-type processes relevant to this work is hard-core processes, which enforce a minimum separation distance between points. Such processes arise naturally when points represent objects of finite size, as is the case for fibers within a composite.

The spatial organization of fiber breaks carries information about load redistribution between fibers and the matrix, as well as the influence of fiber arrangement on damage evolution. Because the governing point process is generally unknown for any observed fracture pattern, this work uses second-order spatial statistics that quantify pairwise structure through the distribution of interpoint separations. The work focuses specifically on two closely related second-order statistics: Ripley's K, which is a cumulative measure of clustering, and the pair correlation function, which is a local measure of clustering.

A complete list of symbols and abbreviations is provided in Table 1.

2.2. Classical Second-Order Spatial Statistics

For *stationary, isotropic* point processes, Ripley's K function is defined as (Ripley, 1977),

$$K(r) = \frac{1}{\lambda}\mathbb{E}[\text{number of further points lying within distance } r \text{ of a typical point}] \tag{2.1}$$

Under CSR, the expected value of $K(r)$ is equal to the size of a d-dimensional domain of radius r,

$$K_{\mathrm{CSR}}(r) = v_d\, r^d \tag{2.2}$$

with $v_1 = 2$, $v_2 = \pi$, and $v_3 = 4\pi/3$. Values of $K(r)$ exceeding this baseline indicate clustering at distances within r, while values below this baseline indicate spatial inhibition.

Ripley's K is a cumulative statistic: it characterizes the distribution of points *within* a given distance from one another. In contrast, the pair correlation function (PCF), $g(r)$, is a local statistic that characterizes spatial dependence *at* a specific separation distance. The PCF is defined in terms of Ripley's K as (Ripley, 1977),

$$g(r) = \frac{1}{a_d r^{d-1}}\frac{dK}{dr} \tag{2.3}$$

where $a_1 = 2$, $a_2 = 2\pi$, and $a_3 = 4\pi$. For a point distribution that follows complete spatial randomness, $g_{CSR}(r) = 1$ for all r. Values above unity indicate clustering, while values less than unity indicate inhibition. Intuitively, $g(r) = A$ means that pairs at separation r occur A times more frequently than expected under CSR.

The functions $K(r)$ and $g(r)$ are theoretical characteristics defined in terms of ensemble expectations. In practice, only finite realizations of a point process are observed, so these quantities must be estimated empirically. Ripley's K is estimated using a weighted pair-counting estimator:

$$K(r) \approx \frac{|D|}{N(N-1)}\sum_{i=1}^{N}\sum_{\substack{j=1\\ j\neq i}}^{N} e_{ij}(r)1\left(r_{ij} \leq r\right) \tag{2.4}$$

where N is the total number of points in the dataset, r_{ij} is the separation distance between points i and j, $e_{ij}(r)$ is an edge correction factor accounting for boundary effects, and 1 is the indicator function. Periodic boundary conditions are used throughout this work, effectively treating the observation domain as a torus; for this case, $e_{ij}(r) = 1$, and the pairwise distances r_{ij} are computed using the minimum image convention. A corresponding pair correlation function estimator follows by binning distances into shells of width Δr centered about r.

In principle, the pair correlation function, $g(r)$, contains more information on second-order point structure than Ripley's K function. As a result, it will be the focus of this work. However, it is important to recognize that $g(r)$ can be noisy for finite N due to binning effects. This is exacerbated at small separation distances, where the number of point pairs is typically lower. Thus, it is imperative to quantify the variability of an estimated $g(r)$, especially when performing hypothesis tests. This is explored in detail in Sections 4 and 5.

2.3. Anisotropic Second-Order Spatial Statistics

Classical second-order statistics are defined for *isotropic* point processes, implicitly assuming that spatial interactions are identical in all directions. Fiber break patterns violate this assumption because breaks only occur along discrete fiber centerlines, and the governing load-transfer processes are directionally dependent. Therefore, this work uses *anisotropic* second-order statistics that separately resolve transverse and axial separations, allowing for decoupling between mechanisms acting in these two principal directions.

Let $r_\perp$ denote transverse separation distance in the plane normal to the fiber axis and $r_\parallel$ denote axial separation along the fiber direction. Assuming isotropy in the transverse plane, an anisotropic Ripley's K can be defined using a cylindrical neighborhood aligned with the fiber axis:

$$K(r_\perp, r_\parallel) = \frac{1}{\lambda}\mathbb{E}[\text{number of further points within } r_\parallel \text{ and } r_\perp \text{ of a typical point}] \tag{2.5}$$

Under CSR, the expected value of this statistic is equal to the volume of the search cylinder,

$$K_{CSR}(r_\perp, r_\parallel) = 2\pi r_\parallel r_\perp^2 \tag{2.6}$$

The corresponding anisotropic PCF is obtained by mixed differentiation in the two principal directions,

$$g(r_\perp, r_\parallel) = \frac{1}{4\pi r_\perp}\frac{\partial^2 K(r_\perp, r_\parallel)}{\partial r_\perp \partial r_\parallel} \tag{2.7}$$

For CSR, $g_{CSR}(r_\perp, r_\parallel) = 1$. Empirical estimators follow from pair counting and binning in $(r_\perp, r_\parallel)$, with the advantage that bin widths in the two principal directions can be chosen independently to manage variance across disparate length scales.

In this work, the pair correlation function is employed in a three-dimensional anisotropic form and in corresponding isotropic reductions in the transverse (2D) and axial (1D) directions. The function $g(r_\perp, r_\parallel)$ is evaluated using a cylindrical neighborhood in $\mathbb{R}^3$. The transverse quantity $g(r_\perp)$ uses a circular neighborhood in $\mathbb{R}^2$, and the axial quantity $g(r_\parallel)$ uses a linear neighborhood in $\mathbb{R}^1$. For values estimated from experimental data, a reported value $g(r_\perp, r_\parallel)$ includes all point pairs whose separations fall within a bin of size $\Delta r_\perp$ and $\Delta r_\parallel$ centered at $r_\perp$ and $r_\parallel$. Going forward, the subscript b is used to denote fiber *break properties*, while the subscript f is used to denote the properties of the *fiber arrangement* in the transverse plane.

3. Fiber Break Spatial Statistics under Global Load Sharing

This section derives analytical expressions for the anisotropic fiber break statistics under two canonical global load-sharing (GLS) models. Although the presentation is framed in the context of ceramic matrix composites, the underlying framework is applicable to any unidirectional fiber-reinforced composite; the single fiber composite (SFC) model, in particular, is directly relevant to polymer matrix composites.

In general, fiber fracture is coupled to matrix cracking and is therefore not spatially random. Stress concentrations near matrix cracks increase the probability of fiber failure in these regions relative to more distant locations (Figure 1A). The resulting fracture patterns can be idealized by two limiting cases: (i) the single fiber composite (SFC) model (Curtin, 1991b), representing a *tough* response characterized by dispersed fiber fragmentation largely independent of matrix cracking (Figure 1B), and (ii) the single matrix crack (SMC) model (Sutcu, 1989), representing a *brittle* response in which fiber fracture is concentrated near a single bridged matrix crack (Figure 1C). These models provide analytically tractable reference states from which the mechanics-based null hypothesis for global load sharing can be derived.

As shown in the following sections, however, the resulting statistical framework is not restricted to these idealized cases. Once the null hypothesis has been established, the fiber interaction statistic applies to arbitrary fiber break distributions, including those that do not conform to either limiting model.

3.1. Single Fiber Composite (SFC) Model

In the SFC limit, the matrix serves to transfer load between fibers and does not contribute to axial load bearing. Under GLS, fiber failures occur independently (Figure 1B). When a fiber breaks, its stress relaxes locally and reloads over a slip length,

$$\delta_f = \frac{\varepsilon E_f R_f}{2\tau_s} \tag{3.1}$$

where ε is the applied strain, E_f is the fiber Young's modulus, R_f is the fiber radius, and τ_s is the interface sliding stress. Because the stress that the fiber experiences is reduced within the slip zone, additional breaks on the same fiber within $\pm\delta_f$ are not permitted.

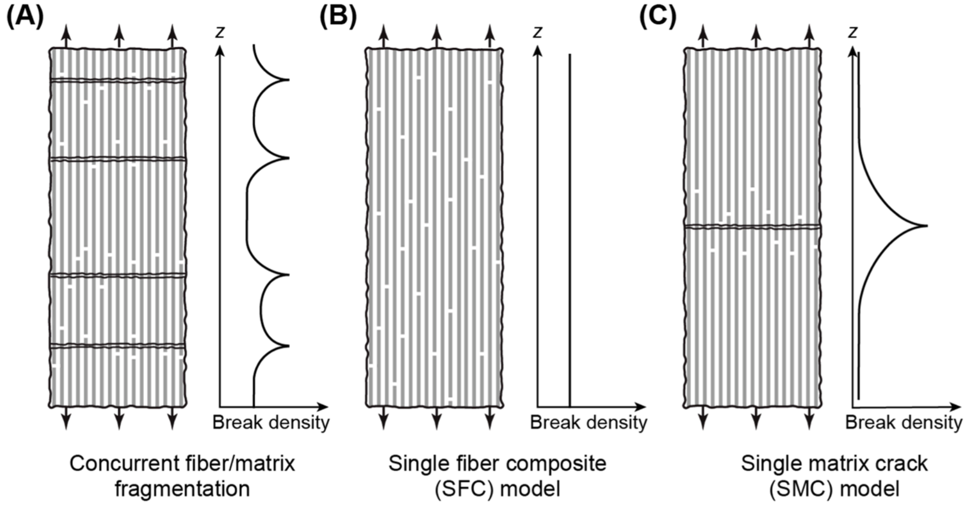

Figure 1. Fiber fracture and break density distributions under global load sharing in three scenarios: (A) during concurrent fiber/matrix fragmentation, (B) in the single fiber composite model, and (C) in the single matrix crack model.

Breaks on an individual fiber are therefore modeled as a stationary one-dimensional hard-core process with minimum separation distance δ_f[1] and average spacing $\bar{l}_b$. An approximate expression for $\bar{l}_b$ is obtained by equating the fractional length of fiber outside of slip zones, $1 - 2\delta_f/\bar{l}_b$, to the survival probability of a segment of length $2\delta_f$, yielding,

$$\frac{\bar{l}_b}{R_f} = \frac{\varepsilon E_f}{\tau_s\left(1 - \exp\left[-\left(\frac{\varepsilon E_f}{\sigma_f^*}\right)^{m+1}\right]\right)} \tag{3.2}$$

where

$$\sigma_f^* = \sigma_f^0\left(\frac{\tau_s L_0}{\sigma_f^0 R_f}\right)^{\frac{1}{m+1}} \tag{3.3}$$

Here σ_f^0 is the reference stress for a reference length L_0 and m is the Weibull modulus.

From Eq. 2.5, Ripley's K function is the expected number of breaks within $r_\perp$ and $r_\parallel$ of a typical break, $\mathbb{E}[n_b]$, normalized by the average break intensity λ_b. Fiber centerlines are modeled as a stationary, isotropic, hard-core point process in $\mathbb{R}^2$ with minimum separation distance $2R_f$. Since the intensity of fiber centers in the transverse plane is $\lambda_f = f/\pi R_f^2$ and the average spacing between breaks on the same fiber is $\bar{l}_b$, it follows that,

$$\lambda_b^{SFC} = \frac{f}{\pi \bar{l}_b R_f^2} \tag{3.4}$$

The expected number of neighboring breaks has two contributions: those on the same fiber, $\mathbb{E}\left[n_b^{sf}\right]$, and those on neighboring fibers, $\mathbb{E}\left[n_b^{nf}\right]$. Since no breaks can occur within δ_f on the same fiber, $\mathbb{E}\left[n_b^{sf}\right]$ is,

$$\mathbb{E}\left[n_b^{sf}\right] = \frac{2\left(r_\parallel - \delta_f\right)^+}{\bar{l}_b} \tag{3.5}$$

where $\left(r_\parallel - \delta_f\right)^+ = \max\left(0, r_\parallel - \delta_f\right)$. $\mathbb{E}\left[n_b^{nf}\right]$ is given by the product of the number of fibers within $r_\perp$, $\mathbb{E}\left[n_f\right]$, and the expected number of breaks along a fiber segment of length $2r_\parallel$, given by $2r_\parallel/\bar{l}_b$. $\mathbb{E}\left[n_f\right]$ is obtained by integrating $g_f(r_\perp)$:

[1] For simplicity, we take δ_f at its current (final) value and ignore the fact that it grows with strain over the loading history. This has essentially no effect on the resulting statistics.

$$\mathbb{E}\left[n_f\right] = 2\pi\lambda_f \int_{2R_f}^{r_\perp} s g_f(s) ds \tag{3.6}$$

It follows, then, that $\mathbb{E}\left[n_b^{nf}\right]$ is,

$$\mathbb{E}\left[n_b^{nf}\right] = 4\pi r_\parallel \frac{\lambda_f}{\bar{l}_b} \int_{2R_f}^{r_\perp} s g_f(s) ds \tag{3.7}$$

Summing the two contributions and normalizing by λ_b^{SFC} yields:

$$K_b^{SFC}(r_\perp, r_\parallel) = \frac{2\pi R_f^2}{f}\left(r_\parallel - \delta_f\right)^+ + 4\pi r_\parallel \int_{2R_f}^{r_\perp} s g_f(s) ds \tag{3.8}$$

From Eq. 2.7, the PCF is obtained through mixed differentiation of K and normalizing by $4\pi r_\perp$. Since the same-fiber term (the first on the right side of Eq. 3.8) is independent of $r_\perp$, its derivative vanishes. Differentiating the second term with respect to both $r_\parallel$ and $r_\perp$ and normalizing yields:

$$g_b^{SFC}(r_\perp, r_\parallel) = g_f(r_\perp) \tag{3.9}$$

Thus, the PCF is governed entirely by the fiber arrangement and is *independent* of $r_\parallel$.

3.2. Single Matrix Crack (SMC) Model

In the SMC limit, a single matrix crack at $z = 0$ produces a triangular fiber stress profile that decays over the matrix slip length,

$$\delta_m = \frac{\sigma_p R_f}{2\tau_s} \tag{3.10}$$

where σ_p is the peak fiber stress in the plane of the crack. Each fiber is permitted to break at most once within the slip zone ($-\delta_m \le z \le \delta_m$). Because the fiber stress varies with z, the axial break distribution is nonuniform but symmetric about $z = 0$. This distribution has been rigorously analyzed (Sutcu, 1989). In the original formulation, the axial break distribution is expressed in terms of a density whose integral over the slip zone yields the fraction of broken fibers, N_b/N_f. Thus, the distribution reflects both the spatial variation in break likelihood and the overall extent of fiber breakage.

However, for second-order spatial statistics, what matters is not how many fibers are broken at each position, but how the likelihood of a break occurring varies along the slip zone. Accordingly, the axial break distribution is recast as a normalized probability density $p_Z\left(z/\bar{l}_p,\ m, N_b/N_f\right)$, defined such that its integral over the slip zone is unity. In this form, p_Z represents the conditional probability of break location given that a break occurs, rather than the spatial distribution of the broken fibers. This distribution depends on the average break distance $\bar{l}_p$ from the matrix crack, the Weibull modulus m, and the composite strain, expressed through

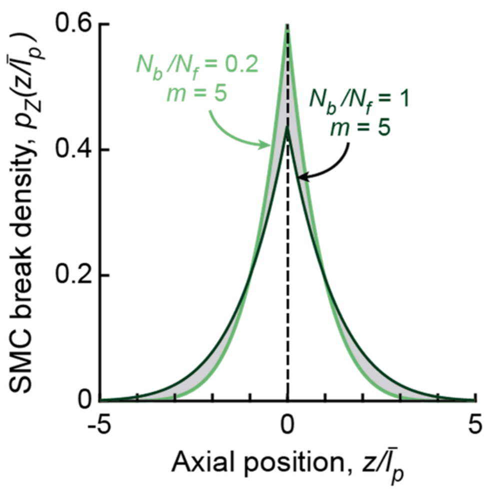

Figure 2. Axial fiber break density for the single matrix crack (SMC) case based on the pullout length distribution derived by Sutcu. Results are shown for fiber Weibull modulus $m = 5$ and broken fiber fraction $N_b/N_f = 0.2$ and 1. All cases with $m \ge 5$ and $N_b/N_f \ge 0.2$ lie within the gray shaded region bounded by these two curves.

the fraction of broken fibers N_b/N_f.

The break density is plotted in Figure 2 for $m = 5$ and $N_b/N_f = 0.2$ and 1. The two curves differ only slightly and bound all distributions for $m \geq 5$ and $N_b/N_f \geq 0.2$ — the domain of practical interest. Consequently, $\bar{l}_p$ emerges as the key parameter governing the axial break density, while m and N_b/N_f play only minor roles; the weak sensitivity to m was also noted by Sutcu in the original derivation.

The average break intensity over the entire domain for a broken fiber fraction N_b/N_f is

$$\lambda_b^{SMC} = \frac{fN_b}{2\pi\delta_m R_f^2 N_f} \tag{3.11}$$

Collapsing the three-dimensional break pattern onto the axial coordinate yields a one-dimensional point process. The probability that a randomly selected fiber contains a break is N_b/N_f, so the probability that a neighbor fiber has a break within an axial distance $r_\parallel$ of a reference break is $P_{\Delta Z}(r_\parallel)N_b/N_f$, where $P_{\Delta Z}(r_\parallel)$ is the CDF of pairwise separations drawn from p_Z. Since the average one-dimensional break density is $N_b/2\delta_m$, the one-dimensional Ripley's K is

$$K_b^{SMC}(r_\parallel) = 2\delta_m P_{\Delta Z}(r_\parallel) \tag{3.12}$$

and the associated one-dimensional PCF is,

$$g_b(r_\parallel) = \delta_m p_{\Delta Z}(r_\parallel) \tag{3.13}$$

where $p_{\Delta Z}$ is the density of pair separations corresponding to p_Z.

Extending to three dimensions, the expected number of neighboring breaks within transverse distance $r_\perp$ and axial distance $r_\parallel$ of a reference break is,

$$\mathbb{E}[n_b] = \frac{2\pi\lambda_f P_{\Delta Z}(r_\parallel)N_f}{N_b}\int_{2R_f}^{r_\perp} s g_f(s)ds \tag{3.14}$$

Normalizing by λ_b^{SMC} (Eq. 3.11) and substituting Eq. 3.12 yields the anisotropic Ripley's K,

$$K_b^{SMC}(r_\parallel, r_\perp) = 2\pi K_b^{SMC}(r_\parallel)\int_{2R_f}^{r_\perp} s g_f(s)ds \tag{3.15}$$

Taking mixed derivatives and using $dK(r)/dr = 2g(r)$ in $\mathbb{R}^1$, the anisotropic PCF becomes

$$g_b^{SMC}(r_\parallel, r_\perp) = g_f(r_\perp)\, g_b^{SMC}(r_\parallel) \tag{3.16}$$

This separability reflects complete decoupling between the transverse fiber arrangement and the axial break correlations, a direct consequence of global load sharing.

3.3. The Fiber Interaction Statistic

When the break distribution exhibits a nonuniform axial density, as in the SMC case, the process is nonstationary. Consequently, conventional second-order statistics reflect both first-order intensity variation and genuine pairwise interactions. In addition, some of these pairwise interactions arise solely from the underlying fiber arrangement rather than mechanical coupling between fibers.

The ultimate objective of this work is to develop a rigorous statistical framework for identifying the presence of, and length scales associated with, spatially autocorrelated fiber break distributions – regardless of the axial break intensity profile. To this end, we introduce a *fiber interaction statistic,* Ψ, that accounts for both first-order axial intensity variation, described by $g_b(r_\parallel)$, and pairwise structure arising from fiber spacing, described by $g_f(r_\perp)$. This statistic is defined as:

$$\Psi(r_\perp, r_\parallel) = \frac{g_b(r_\perp, r_\parallel)}{g_f(r_\perp)g_b(r_\parallel)} \tag{3.17}$$

Because $g_b(r_\parallel)$ is normalized out explicitly rather than assumed, Ψ tests for departures from global load sharing irrespective of the underlying axial break intensity profile. The SFC and SMC models, corresponding to a uniform ($g_b(r_\parallel) = 1$) and a localized profile, respectively, are presented as two tractable limiting cases for which $g_b(r_\parallel)$ can be derived analytically. However, Ψ applies equally to any other axial profile, including those arising from finite-fiber damage localization near final composite fracture (Curtin, 1993; Callaway and Zok, 2020), or any break pattern not captured by these idealized limiting cases (Figure 1A).

Under the global load-sharing null hypothesis, $\mathbb{E}[\Psi(r_\perp, r_\parallel)] = 1$. Deviations from unity indicate coupling between transverse and axial break separation distances, providing evidence of autocorrelated fiber fracture at a particular length scale. Intuitively, $\Psi(r_\perp, r_\parallel) = A$ means that fibers separated by $r_\perp$ are A times more likely to have break pairs with axial separation $r_\parallel$ than would be expected under the global load-sharing null hypothesis.

The key advantage of $\Psi(r_\perp, r_\parallel)$ is that it explicitly normalizes the PCF for both the transverse fiber arrangement and the axial break intensity profile. Since these components can vary substantially from sample to sample, their removal isolates the interaction structure arising from fiber-to-fiber load transfer. Therefore, for break distributions in which the load-sharing characteristics are expected to be similar—obtained, for example, from multiple finite element simulations with the same composite properties or experimental measurements on multiple composite specimens produced in a nominally equivalent manner—$\mathbb{E}[\Psi(r_\perp, r_\parallel)]$ is *independent* of fiber volume fraction, fiber arrangement, specimen length probed, and axial break profile. This makes Ψ a robust statistic for cross-sample comparison and for hypothesis testing of spatially autocorrelated fiber fracture. The variability and statistical power of $\Psi(r_\perp, r_\parallel)$ is explored in detail in the following sections.

4. Monte Carlo Simulations under Global Load Sharing

4.1. Preliminaries

The preceding section presents results for anisotropic second-order spatial statistics of fiber breaks under GLS for both the SFC and SMC cases. These results provide null hypotheses for the expected PCF in infinitely large samples. In practice, however, fracture patterns are observed over a finite gauge length with a finite number of fibers. Even when the underlying fracture process exactly satisfies the GLS null model, $g_b(r_\perp, r_\parallel)$ and $\Psi(r_\perp, r_\parallel)$ exhibit intrinsic variability due to finite sampling. Consequently, meaningful inference requires quantifying the estimator uncertainty for realistic composite properties and sample size.

The objective here is to characterize *finite-sample variability* of the anisotropic PCF and the interaction statistic Ψ through Monte Carlo simulations. Monte Carlo simulations provide a controlled means of generating synthetic fracture patterns with known governing assumptions, enabling separation of true departures from the null hypothesis from fluctuations due to finite observation. One outcome is the minimum requirements on sample size to achieve reliable statistical inference.

For the uncertainty quantification presented here, periodic boundary conditions (PBC) are used to isolate variance attributable to finite sample size alone. While PBC is not generally appropriate for experimental datasets, it provides a consistent baseline noise level that is not confounded by sample-dependent edge artifacts.

While the second-order statistics can, in principle, be computed over the entire $r_\perp$ and $r_\parallel$ domain, only those at small separation distances are of interest. This is because local load sharing is only expected to manifest over short transverse distances, on the order of a few fiber diameters (Han et al., n.d.). Consequently, the focus will be on the domain $2R_f \le r_\perp \le 10R_f$. In the forthcoming section, the estimator uncertainty is related to system size (number of fibers, number of observed breaks, probed gauge length) and composite properties (average break spacing for SFC and average break distance for SMC). Variance also depends on bin widths $\Delta r_\perp$ and $\Delta r_\parallel$, which control the tradeoff between resolution and noise. These effects are also examined in detail.

As discussed in Section 3, the second-order statistics of fiber break patterns depend on the underlying fiber arrangement, characterized by $g_f(r_\perp)$. However, the fiber interaction statistic Ψ explicitly accounts for fiber arrangement through normalization by $g_f(r_\perp)$. As such, the mean values of Ψ should be universal for any composite with similar load-transfer characteristics, *independent* of $g_f(r_\perp)$.

While the expected value of Ψ is independent of the fiber arrangement, its sampling variance is not. The variance of Ψ depends on the local packing statistics, which is described by $g_f(r_\perp)$. Consequently, variability of the estimator will reflect the underlying microstructural statistics to some extent.

4.2. Generating Fiber Arrays

For the Monte Carlo simulations, fiber arrangements and fiber fracture patterns are generated in $\mathbb{R}^3$. Fibers are modeled as straight

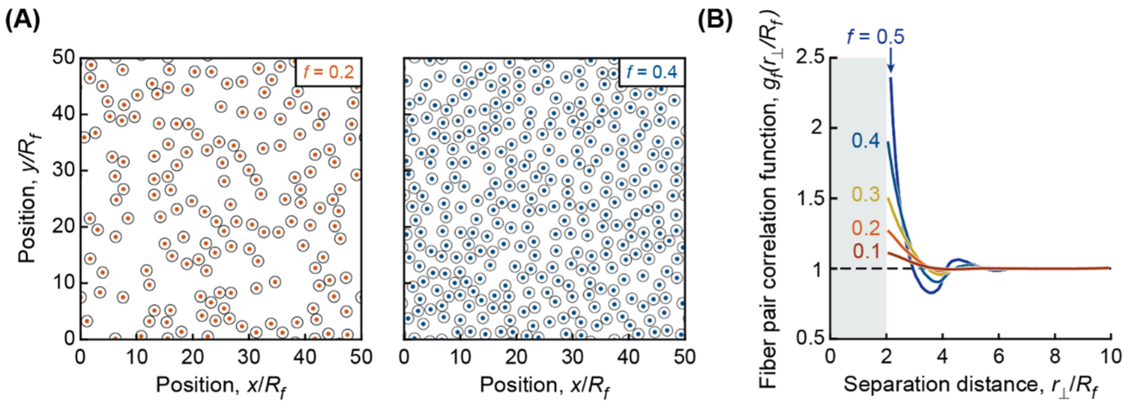

Figure 3. Spatial statistics of simulated composite microstructures generated using simple sequential inhibition (SSI). (A) Representative randomized microstructures for fiber volume fraction $f = 0.2$ (left) and $f = 0.4$ (right) in a $50R_f \times 50R_f$ square with periodic boundary conditions. (B) Pair correlation functions for fiber volume fractions $f = 0.1,\ 0.2,\ 0.3,\ 0.4$, and 0.5. Curves show ensemble averages over 5,000 realizations of 500 fibers each. The dashed line denotes complete spatial randomness (CSR).

aligned cylinders of radius R_f. Each realization contains $N_f = 500$ fibers (representing a typical individual tow) within a square cross-sectional domain. The domain side length is chosen to achieve the prescribed fiber volume fraction f. Fiber center positions are generated using a homogeneous Simple Sequential Inhibition (SSI) hard-core point process in $\mathbb{R}^2$ with periodic boundary conditions. The hard-core constraint enforces the minimum permissible fiber spacing dictated by the fiber radius.

SSI point processes exhibit nontrivial short-range order due to packing effects. Figure 3A shows representative SSI realizations of fibers in a $50R_f \times 50R_f$ domain with PBC for $f = 0.2$ and 0.4. Ensemble average fiber pair correlation functions $g_f(r_\perp)$ are presented for several fiber volume fractions in Figure 3B. As the fiber volume fraction approaches the two-dimensional SSI saturation limit of $f \approx 0.547$, peaks and valleys form at small separation distances, corresponding to clustering and inhibition due to point jamming. This characteristic of SSI processes has been well documented in previous studies (Boyer et al., 1995).

4.3. Single Fiber Composite Simulations

The single fiber composite (SFC) simulations are parameterized by the fiber radius R_f, fiber volume fraction f, mean break spacing $\bar{l}_b$, slip length δ_f, and composite gauge length L. Each Monte Carlo realization begins by generating a unique fiber arrangement using SSI in $\mathbb{R}^2$ consistent with the prescribed f and R_f. The number of breaks on each fiber is then drawn independently from a Poisson distribution with mean $L/\bar{l}_b$. The expected number of breaks per realization is therefore,

$$\mathbb{E}[N_b] = N_f \frac{L}{\bar{l}_b} \tag{4.1}$$

where N_f is the number of fibers. After assigning the number of breaks to each fiber, axial break locations are generated using an SSI hard-core point process in $\mathbb{R}^1$ with minimum separation distance δ_f. The break pair correlation function and the fiber interaction statistic are then estimated for each realization.

Two characteristic length scales govern the anisotropic statistics: fiber radius R_f in the transverse direction and mean break spacing $\bar{l}_b$ in the axial direction. Accordingly, $r_\perp$ and $\Delta r_\perp$ are normalized by R_f while $r_\parallel$ and $\Delta r_\parallel$ are normalized by $\bar{l}_b$.

Figure 4 shows results generated using $N_f = 500$, $f = 0.4$, $\bar{l}_b = 500R_f$, $L = 2\bar{l}_b$, and $\delta_f = 50R_f$. These values were chosen to give a realistic break density for a typical SiC/SiC composite containing a single fiber tow strained to approximately 0.5% (Eq. 3.2), producing an average of 1,000 breaks per realization. Unless otherwise noted, all quantities were computed using bin widths $\Delta r_\perp = 0.25R_f$ and $\Delta r_\parallel = 0.05\bar{l}_b = 25R_f$.

Figure 4A shows a heatmap of the ensemble mean of g over 500 realizations. Although two-dimensional heatmaps provide a complete view of mean behavior, they are not ideal for uncertainty visualization or comparison between datasets. In practice, one-dimensional slices provide a clearer basis for hypothesis testing. Thus, representative slices of both g_b and Ψ evaluated at $r_\parallel = 0.05\bar{l}_b$ (the first axial bin) are shown in Figures 4B and 4C, respectively. As expected, g_b exhibits transverse structure consistent with the underlying fiber pair correlation function $g_f(r_\perp)$ at small $r_\perp$ and trends towards complete spatial randomness at large $r_\perp$. The estimator exhibits excellent agreement with the analytical solution, indicating that it is unbiased. The interaction statistic $\Psi(r_\perp, r_\parallel)$ likewise agrees closely with the null hypothesis of $\Psi = 1$ over the entire range of $r_\perp$. The corresponding 95% confidence intervals on the Monte Carlo ensemble averages (shown by shaded bands) exhibit widths of approximately 3.92 times the standard deviation of their respective quantities, consistent with Gaussian estimator distributions.

To quantify the dependence of the standard deviation of Ψ on sample size and composite properties, a parametric study was conducted with the following sweep:

$$f = [0.1,\ 0.2,\ 0.3,\ 0.4,\ 0.5];\ N_f = [200,\ 500,\ 800];\ \bar{l}_b/R_f = [250,\ 500,\ 1{,}000];$$

$$L/\bar{l}_b = [2,\ 3.5,\ 5]; \Delta r_\perp/R_f = [0.01,\ 0.1,\ 0.25,\ 0.5,\ 1],\ \Delta r_\parallel/\bar{l}_b = [0.01, 0.05,\ 0.1,\ 0.25,\ 0.5,\ 1]$$

for a total of 4,050 combinations. For each parameter combination, the standard deviation of the fiber interaction statistic across 100 realizations was computed. From this study, the standard deviation was found to scale as,

$$SD[\Psi(r_\perp, r_\parallel)] \propto \left(f N_f \frac{L}{\bar{l}_b} \frac{r_\perp}{R_f} \frac{\Delta r_\perp}{R_f} \right)^{-1/2} \tag{4.2}$$

Equivalently, in terms of the number of observed fiber breaks N_b,

$$SD[\Psi(r_\perp, r_\parallel)] \propto \left(f N_b \frac{r_\perp}{R_f} \frac{\Delta r_\perp}{R_f} \right)^{-1/2} \tag{4.3}$$

These results indicate that doubling the probed gauge length of the composite (or equivalently the number of observed breaks) reduces statistical uncertainty by a factor of $\sqrt{2}$, or 29%. Likewise, for a fixed sample size, the same improvement is achieved by doubling the transverse bin width.

Figure 4D shows a plot of $SD[\Psi(r_\perp, r_\parallel)]$, normalized by the quantity in Eq. 4.3, as a function of $\Delta r_\parallel/\bar{l}_b$. Across the 675 parameter

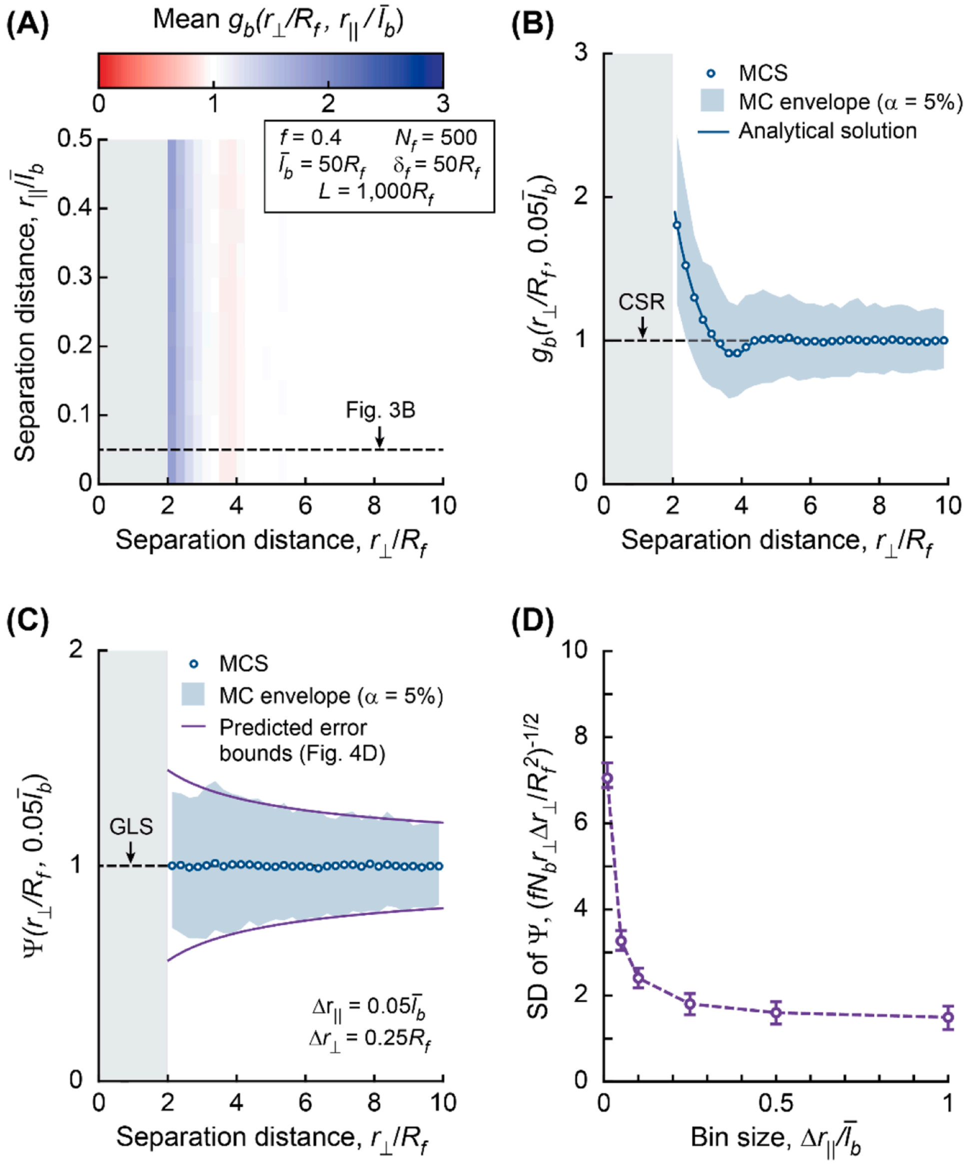

Figure 4. Second-order spatial statistics for a single fiber composite (SFC) with simulation parameters listed in (A). Unless otherwise noted, all quantities are computed using the bin size listed in (C). (A) Ensemble mean estimated pair correlation function, g_b, from 500 realizations. Red indicates inhibition, blue indicates clustering, and white corresponds to complete spatial randomness (CSR). (B) Slice of the anisotropic pair correlation function at $r_{\|} = 0.05\bar{l}_b = 25R_f$. Circles denote ensemble means from (A), and the shaded region represents the 95% Monte Carlo envelope. The solid line shows the analytical solution, and the dashed line indicates CSR. (C) Slice of the normalized interaction statistic, Ψ, at $r_{\|} = 0.05\bar{l}_b$. Circles denote ensemble means, and the shaded region represents the 95% Monte Carlo envelope. The dashed line indicates the global load-sharing (GLS) null hypothesis. Solid purple lines show the predicted two-sided $\alpha = 5\%$ error bounds, assuming normally distributed values with standard deviation determined from the mean value corresponding to $\Delta r_{\|} = 0.05\bar{l}_b$ in (D). (D) Standard deviation of Ψ in normalized units as a function of axial bin size. Circles denote mean values, and error bars span the minimum and maximum values across the full parameter study.

combinations evaluated for each axial bin width, the normalized distributions collapse tightly, confirming the robustness of the proposed scaling. Increasing the axial bin size does reduce variance, but diminishing returns occur as $\Delta r_{\|}$ approaches $\bar{l}_b$. This is because, as $\Delta r_{\|}$ gets large, essentially every fiber is represented within a bin. Further increasing $\Delta r_{\|}$, then, does not introduce new transverse separation distances, despite adding new axial pairs; as such, variability becomes controlled by the finite number of fibers rather than the number of axial counts per bin. In this limit, the normalized $SD[\Psi]$ approaches 1.3.

Figure 4D yields a practical tool for estimating $SD[\Psi]$ without the need for Monte Carlo simulations. In Figure 4C, 95% confidence intervals were estimated using the mean normalized standard deviation from Figure 4D at $\Delta r_{\|} = 0.05\bar{l}_b$. These predictions closely match the 95% confidence intervals of the Monte Carlo ensemble envelope. Similar agreement was observed across a wide range of simulation parameters. This result demonstrates that reliable uncertainty bounds for the GLS null hypothesis can be predicted from sample size and composite properties alone, through a combination of Eq. 4.3 and the empirically derived normalized $SD[\Psi]$ of 1.3.

4.4. Single Matrix Crack Simulations

The SMC simulations are parameterized by the fiber radius R_f, fiber volume fraction f, the matrix slip length δ_m, the average break distance $\bar{l}_p$, the Weibull modulus m, and the fraction of broken fibers N_b/N_f. As breaks only occur within $(-\delta_m \leq z \leq \delta_m)$, the com-

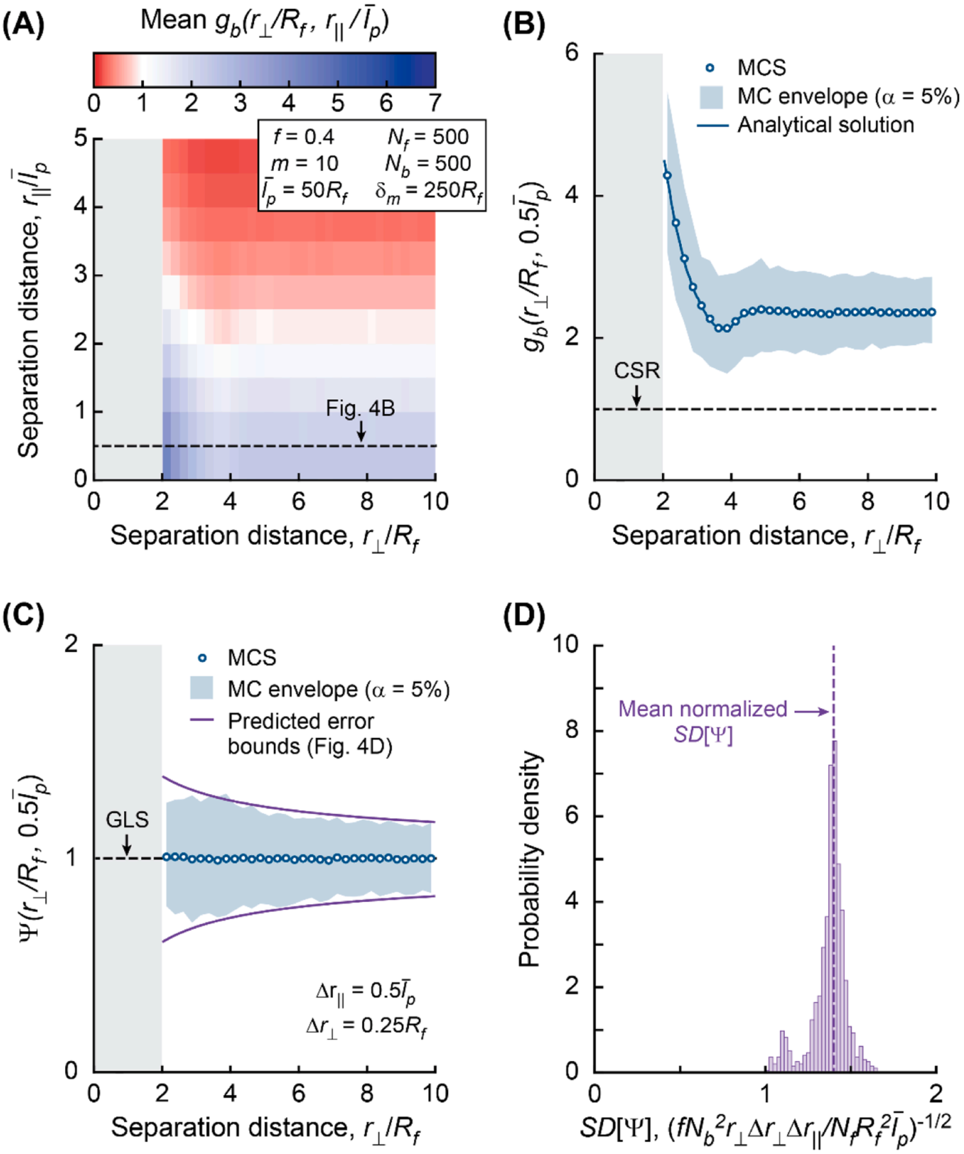

Figure 5. Second-order spatial statistics for a single matrix crack (SMC) with simulation parameters listed in (A). Unless otherwise noted, all quantities are computed using the bin size listed in (C). (A) Ensemble mean estimated pair correlation function, g_b, from 500 realizations. Red indicates inhibition, blue indicates clustering, and white corresponds to complete spatial randomness (CSR). (B) Slice of the anisotropic pair correlation function at $r_{||} = 0.5\bar{l}_p = 25R_f$. Circles denote ensemble means from (A), and the shaded region represents the 95% Monte Carlo envelope. The solid line shows the analytical solution, and the dashed line indicates CSR. (C) Slice of the normalized interaction statistic, Ψ, at $r_{||} = 0.5\bar{l}_p$. Circles denote ensemble means, and the shaded region represents the 95% Monte Carlo envelope. The dashed line indicates the global load-sharing (GLS) null hypothesis. Solid purple lines show the predicted two-sided $\alpha = 5\%$ error bounds, assuming normally distributed values with standard deviation determined from the mean value corresponding to $\Delta r_{||} = 0.5\bar{l}_p$ in (D). (D) Standard deviation of Ψ in normalized units, with the mean value across the entire parameter sweep indicated by the dashed line.

posite gauge length is set to $L = 2\delta_m$.

For each realization, a unique fiber arrangement consistent with the prescribed R_f and f is generated through SSI. N_b random axial positions are then chosen from $p_Z(z/\bar{l}_p, m, N_b/N_f)$, and each break location is randomly assigned to a different fiber. Then, empirical estimates of the PCF and Ψ are computed. Here, $r_\perp$ is normalized by R_f while $r_\parallel$ is normalized by $\bar{l}_p$, as these are the characteristic length scales in their respective directions.

Figure 5 shows simulation results for parameter values: $N_f = 500, f = 0.4, m = 5, N_b/N_f = 1$ and $\bar{l}_p = 50R_f$. These properties were chosen to represent a typical single-tow SiC/SiC composite that has been strained to failure (Eq. 3.10). Since the concentration of breaks more than $5\bar{l}_p$ away from the matrix crack is negligible (as shown in Figure 2), δ_m is selected to be $\delta_m = 5\bar{l}_p = 250R_f$. All quantities are plotted with bin widths $\Delta r_\perp = 0.25R_f$ and $\Delta r_\parallel = 0.5\bar{l}_p = 25R_f$.

Figure 5A shows a heatmap of the mean PCF over 500 realizations. The PCF is essentially independent of $r_\perp$, with the exception of the region near $2R_f < r_\perp < 4R_f$, where an increased level of clustering arises from the fiber arrangement, as demonstrated earlier in Figure 3B. This is evidenced by the white band in the PCF at moderate $r_\parallel$. For large values of $r_\parallel$, the PCF approaches zero as the concentration of breaks far away from the matrix crack is very small, making separation distances above $r_\parallel \approx 2\bar{l}_p$ very unlikely.

Representative slices of g_b and Ψ evaluated at $r_\parallel = 0.25\bar{l}_p$ are shown in Figures 5B and 5C, respectively. The mean values exhibit excellent agreement with the analytical solution, confirming unbiased estimation. Additionally, as in the SFC simulations, the width of the 95% Monte Carlo envelope indicates that the estimator distributions are approximately Gaussian.

A parametric study, similar to the one for the SFC, was performed to quantify the standard deviation of Ψ. The parameter sweep was as follows:

$$f = [0.1,\ 0.2,\ 0.3,\ 0.4,\ 0.5];\ N_f = [200,\ 500,\ 800];\ \bar{l}_p/R_f = [100,\ 250,\ 500];$$

$$N_b/N_f = [0.2,\ 0.5,\ 1];\ \Delta r_\perp/R_f = [0.01,\ 0.1,\ 0.25,\ 0.5,\ 1];\ \Delta r_\parallel/\bar{l}_p = [0.05,\ 0.1,\ 0.25,\ 0.5,\ 1]$$

$$m = [5,\ 10,\ 15]$$

for a total of 10,125 combinations. The analysis focuses on small axial separation distance ($r_\parallel \le \bar{l}_p$), as this is where most points lie. The results show that the standard deviation of Ψ scales as:

$$SD[\Psi(r_\perp, r_\parallel)] \propto \left(f N_b \frac{N_b}{N_f} \frac{r_\perp}{R_f} \frac{\Delta r_\perp}{R_f} \frac{\Delta r_\parallel}{\bar{l}_p} \right)^{-1/2} \tag{4.4}$$

with essentially no dependence on m or $r_\parallel$ (for $r_\parallel \le \bar{l}_p$). This result is similar to that for the SFC case, but with two additional terms: the fraction of broken fibers N_b/N_f and the axial bin width $\Delta r_\parallel/\bar{l}_p$, both of which increase the SD. The contribution of $\Delta r_\parallel/\bar{l}_p$ arises directly from the axial intensity variation inherent to the SMC. The distribution of $SD[\Psi]$ normalized by the quantity in Eq. 4.4 is plotted in Figure 5D; its average value is approximately 1.4, with all results falling in the range 1.0–1.7. The utility of this normalization for predicting error bands is demonstrated in Figure 5C.

5. Analysis of Spatially Correlated Fiber Fracture

To assess whether the proposed null hypotheses and the fiber interaction statistic Ψ can detect deviations from global load sharing, we construct a deliberately simple synthetic dataset with controlled, spatially correlated fiber fracture. The objective is not to reproduce a fully physical local load-sharing model, but rather to introduce a minimal and transparent perturbation to the SFC and SMC frameworks that generates measurable short-range correlation. If the statistical measures developed in the previous sections are sensitive to local load transfer, they should detect this perturbation unambiguously.

5.1. Single Fiber Composite Model

As a first test case, we adapt the baseline SFC Monte Carlo simulation described in Section 4.3. To introduce spatial autocorrelation in fracture events, a triggered-break mechanism is added in the following way:

(i) After generating the transverse fiber array using SSI, all fiber–fiber separation distances are computed. Only fiber pairs with transverse separation $r_\perp \le 2.25R_f$ are considered eligible for triggered failure, ensuring that correlations occur exclusively between immediately adjacent fibers. For the SSI fiber arrangements used in this study, approximately one in five fibers at $f = 0.2$ are expected to have at least one eligible neighbor; at $f = 0.4$, this increases to almost half of all fibers.

(ii) A subset corresponding to a prescribed fraction p_t of the eligible fiber pairs is then selected for triggered events. For each selected pair, a break is placed on both fibers at an identical[2] axial position drawn from $z \sim U[0, L]$. If a fiber appears in multiple

[2] As the estimators have an axial bin width of $\Delta r_\parallel$, this is equivalent to triggered breaks occurring within $0 \le r_\parallel \le \Delta r_\parallel$ of one another.

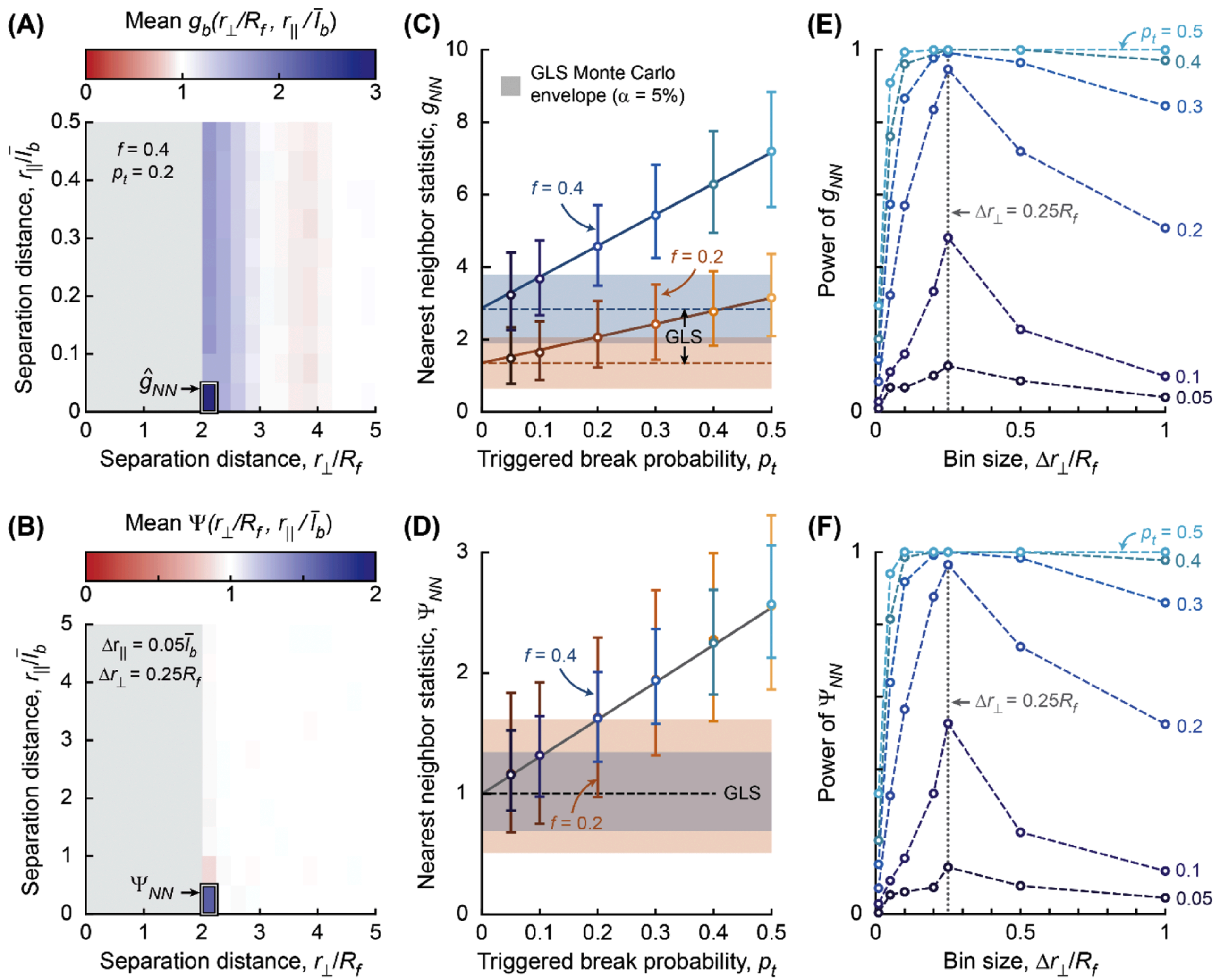

Figure 6. Anisotropic second-order spatial statistics for SFC-type Monte Carlo simulations with spatially autocorrelated fiber fracture (parameters as in Figure 4 unless otherwise noted). Ensemble mean (A) pair correlation function and (B) normalized interaction statistic computed from 500 realizations with fiber volume fraction $f = 0.4$ and triggered-break probability $p_t = 0.2$. White indicates CSR for the pair correlation function and GLS for the normalized interaction statistic; blue denotes values above, and red denotes values below, the respective null expectations. Boxed bins identify the nearest-neighbor statistics g_{NN} and Ψ_{NN}. Nearest-neighbor statistics (C) g_{NN} and (D) Ψ_{NN} plotted as functions of triggered-break probability, p_t, for $f = 0.2$ and 0.4, using the same bin size as in (A) and (B). Circles indicate ensemble means, and error bars represent the 2.5th and 97.5th percentiles from the Monte Carlo simulations. Dashed lines and shaded regions denote the expected values and 95% Monte Carlo envelopes, respectively, under the GLS null hypothesis. (E) Statistical power ($\alpha = 0.05$) of g_{NN} and (F) Ψ_{NN} for detecting deviations from the GLS null hypothesis as a function of transverse bin size, shown for $f = 0.4$ and multiple triggered-break probabilities p_t.

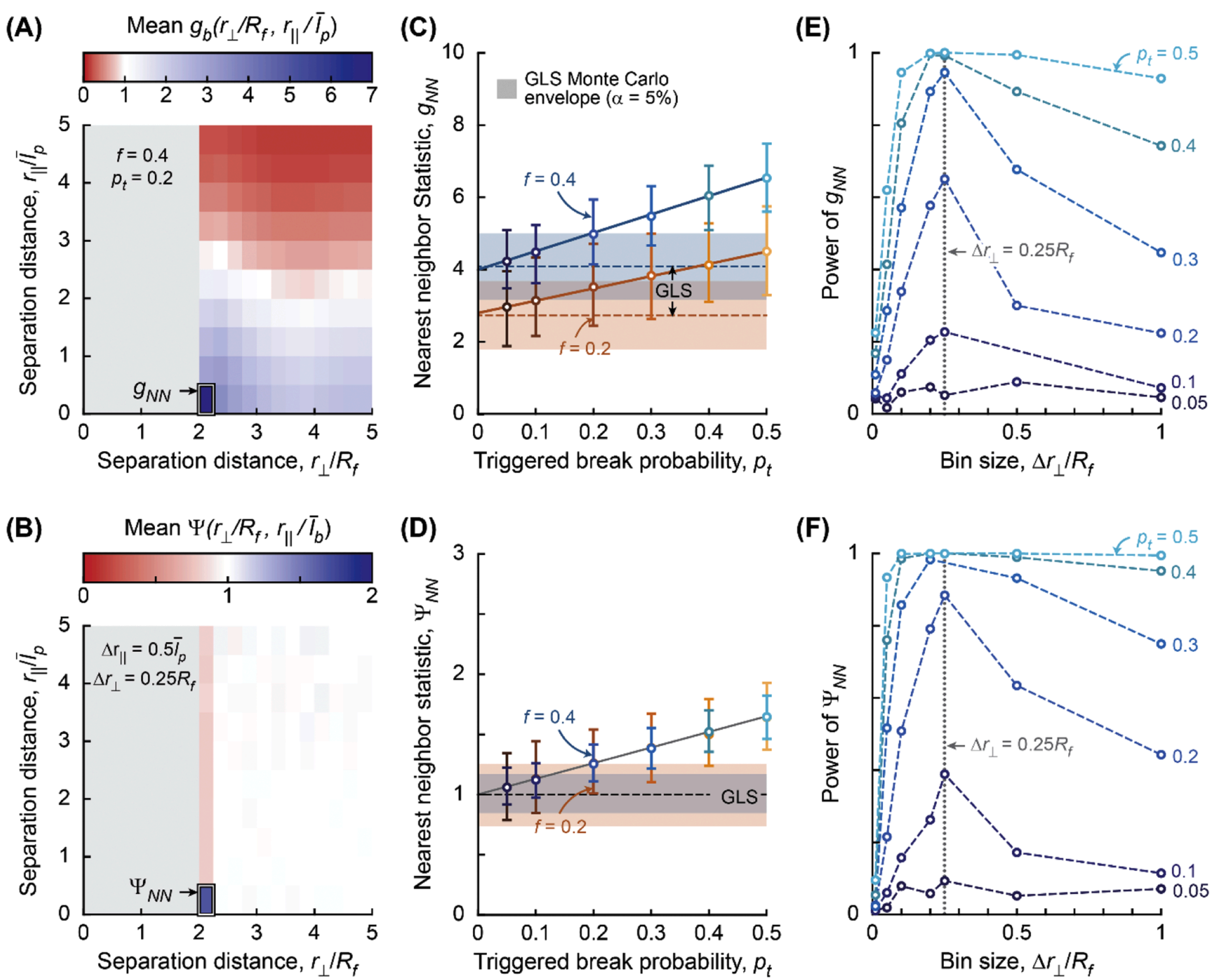

Figure 7. Anisotropic second-order spatial statistics for SMC-type Monte Carlo simulations with spatially autocorrelated fiber fracture (parameters as in Figure 5 unless otherwise noted). Ensemble mean (A) pair correlation function and (B) normalized interaction statistic computed from 500 realizations with fiber volume fraction $f = 0.4$ and triggered-break probability $p_t = 0.2$. White indicates CSR for the pair correlation function and GLS for the normalized interaction statistic; blue denotes values above, and red denotes values below, the respective null expectations. Boxed bins identify the nearest-neighbor statistics g_{NN} and Ψ_{NN}. Nearest-neighbor statistics (C) g_{NN} and (D) Ψ_{NN} plotted as functions of triggered-break probability, p_t, for $f = 0.2$ and 0.4, using the same bin size as in (A) and (B). Circles indicate ensemble means, and error bars represent the 2.5th and 97.5th percentiles from the Monte Carlo simulations. Dashed lines and shaded regions denote the expected values and 95% Monte Carlo envelopes, respectively, under the GLS null hypothesis. (E) Statistical power ($\alpha = 0.05$) of g_{NN} and (F) Ψ_{NN} for detecting deviations from the GLS null hypothesis as a function of transverse bin size, shown for multiple triggered-break probabilities p_t.

selected pairs, a cascade occurs in which all fibers in the connected cluster break at the same axial position. Consequently, each fiber can participate in at most one triggered event. This procedure is repeated until all triggered events have been assigned.

(iii) Finally, the remaining independent breaks are generated following the procedure described in Section 4.3. This procedure ensures that the total number of breaks and overall break density remain consistent with the GLS baseline, while introducing a controlled fraction of short-range, axially coincident break pairs.

The anisotropic second-order statistics from these simulations are presented in Figure 6. Because the imposed spatial correlation is restricted to $r_\perp \leq 2.25R_f$, only small transverse separation distances (up to $5R_f$) are shown. Unless otherwise noted, all simulation parameters and bin sizes are identical to those used in Section 4.3.

Figures 6A and 6B show heatmaps of the ensemble averages of $g(r_\perp, r_\parallel)$ and $\Psi(r_\perp, r_\parallel)$ for $p_t = 0.2$ over 500 realizations. Outside of the first few bins at very small separation distances, the heatmaps are nearly indistinguishable from the GLS null hypotheses. In contrast, in the bins corresponding to $r_\parallel \leq 0.05\bar{l}_b$ and $r_\perp \leq 2.25R_f$, the spatial autocorrelation manifests as pronounced clustering in g and significant deviation from the GLS null hypothesis in Ψ.

The axial bins immediately above these show anticorrelation in Ψ, reflecting the increased likelihood that neighboring fibers break at nearly identical axial positions, thereby reducing the probability of nearby but noncoincident axial breaks. At larger axial separations, Ψ approaches unity. Because each fiber can participate in only one triggered cluster, the imposed LLS signature becomes increasingly difficult to detect once separations corresponding to multiple breaks per fiber are probed.

To quantify statistical sensitivity, SFC Monte Carlo simulations were performed with triggered-break fractions p_t ranging from 0.05 to 0.50. The analysis focused on the nearest-neighbor bin, defined by $2R_f \leq r_\perp < 2R_f + \Delta r_\perp$ and $0 \leq r_\parallel < 0.05\bar{l}_b$, where deviations from GLS are expected to be strongest. The corresponding statistics in this bin are denoted g_{NN} and Ψ_{NN}. Results are plotted on Figures 6C and 6D for fiber volume fractions $f = 0.2$ and 0.4. Notably, while g_{NN} increases with both p_t and f, Ψ_{NN} depends only on p_t. This demonstrates the utility of Ψ_{NN} for comparing samples with differing fiber volume fractions. However, the variance of both g_{NN} and Ψ_{NN} increases at lower fiber volume fractions due to the reduced number of fiber–fiber pairs at small $r_\perp$.

For each value of $\Delta r_\perp$, null distributions were obtained from 500 realizations with $p_t = 0$. A two-sided rejection region at significance level $\alpha = 0.05$ was defined from the empirical 2.5th and 97.5th percentiles. By construction, this yields an approximate 5% false positive rate under GLS conditions, confirming proper calibration. For $p_t > 0$, the proportion of realizations exceeding this threshold was recorded as the statistical power (true positive rate). The resulting power curves for g_{NN} and Ψ_{NN} are shown in Figures 6E and 6F for $f = 0.4$. Both statistics perform similarly, with Ψ_{NN} exhibiting slightly higher power than g_{NN} (by 1–5%). This reflects the ability of Ψ_{NN} to control for microstructural variability, thereby reducing baseline variance. Across all values of p_t, power is maximized when $\Delta r_\perp$ is comparable to the imposed transverse correlation scale of $0.25R_f$. In this case, nearly all triggered nearest-neighbor pairs are captured without excessive dilution from uncorrelated breaks. As $\Delta r_\perp$ increases further, additional uncorrelated interactions are included, lowering power.

The peak power of Ψ_{NN} for the SFC case is over 95% for $p_t \geq 0.2$. This is a significant result, as $p_t = 0.2$ corresponds to only about 4% of breaks per realization being statistically correlated at $f = 0.4$; even at $p_t = 0.1$ (where roughly 2% of breaks are correlated), Ψ_{NN} achieves a power of about 50% at the optimal bin size.

5.2. Single Matrix Crack Model

As a second test case, the triggered-break mechanism was superimposed on the SMC simulation described in Section 4.4. Unlike SFC, SMC does not permit multiple breaks on the same fiber; therefore, once a fiber experiences a triggered break, it becomes ineligible for an additional (independent) break. Aside from this difference, the triggered-break procedure is identical, with axial break positions drawn from the distribution derived by (Sutcu, 1989).

The results of these simulations are shown in Figure 7. Simulation parameters are identical to those in Section 4.4 unless otherwise stated, with $p_t = 0.2$. The mean values of g and Ψ are shown by the heatmaps in Figures 7A and 7B. As in the SFC case, deviations from GLS occur only at small separation distances. However, Ψ exhibits greater noise at large $r_\parallel$ due to the limited number of breaks at large axial separations. The first few bins show strong clustering in g and pronounced deviation from GLS in Ψ. Unlike the SFC case, anticorrelation in Ψ persists across all axial bins beyond the first, reflecting the absence of same-fiber breaks.

Figures 7C and 7D show the effects of p_t on g_{NN} and Ψ_{NN} for $f = 0.2$ and 0.4. Compared with the SFC case, the mean values of Ψ are lower for a given p_t, since Ψ effectively measures the number of observed breaks relative to the expected number. Because SMC exhibits more breaks with small axial separation distances, the number of expected breaks in this nearest-neighbor bin is larger. As a result, Ψ takes a smaller value for the same p_t than in the SFC case.

As in the SFC case, g_{NN} increases with both p_t and f, whereas Ψ_{NN} depends only on p_t, again confirming the effectiveness of the normalization (Eq. 3.17). However, the variances of both g_{NN} and Ψ_{NN} increase at lower fiber volume fractions because the number of fiber–fiber pairs at small $r_\perp$ is reduced.

Figures 7E and 7F show the statistical power analysis. The peak statistical power for both statistics again occurs when $\Delta r_\perp \approx 0.25R_f$. Detection performance is moderately worse in SMC compared to SFC; this is because the axial profile varies much more strongly between realizations in SMC than in SFC, and the number of observed breaks is half that in the SFC simulation due to the absence of same-fiber breaks. Moreover, Ψ significantly outperforms g in SMC, whereas the difference between the two statistics is modest in SFC. This reflects the fact that Ψ controls for both the axial stress variation and the variability in fiber arrangement (Eq. 3.17). Because the axial profile is more pronounced in SMC than in SFC, the normalization reduces noise more effectively relative to g. For $p_t =$

0.2—where only 8% of breaks are correlated—Ψ_{NN} has a power of about 75%; for $p_t = 0.1$, this decreases to around 40%.

6. Discussion

6.1. Mechanics-Based Spatial Statistics

The central contribution of this work is a mechanics-based statistical framework for inferring load-transfer interactions from three-dimensional damage data. Such inverse problems are becoming increasingly important as modern volumetric imaging techniques provide unprecedented access to the three-dimensional evolution of damage in heterogeneous materials. In these systems, the observed spatial organization of damage reflects three superposed contributions: the arrangement of potential event sites, the nonuniform intensity of events, and any mechanical coupling between events. Extracting mechanics from experimental observations therefore requires that these contributions be analyzed separately.

Unidirectional fiber-reinforced composites provide a particularly well-posed example of such problems. The potential event sites are the fiber centerlines, whose arrangement is directly measurable; the axial break intensity is likewise directly measurable and, in some cases, derivable analytically; and the load-transfer mechanisms are sufficiently well understood to analytically derive a mechanics-based reference state corresponding to mechanical independence. The anisotropic decomposition is central to this framework. Load recovery along a broken fiber occurs through interfacial shear over the slip length, whereas transverse load transfer occurs through the surrounding matrix over a much shorter characteristic distance. Decomposing pairwise separations into axial and transverse components therefore maps the statistics directly onto these distinct physical mechanisms; statistics that conflate the two directions necessarily lose this correspondence.

The most significant theoretical result is that, under global load sharing, the pair correlation function is separable in axial and transverse coordinates. This separability establishes a mechanics-based null hypothesis for mechanical independence among fibers that is fundamentally different from the complete spatial randomness commonly adopted in classical point-process analysis. Departures from separability indicate coupling between transverse and axial fracture processes and therefore provide a direct statistical signature of local load sharing.

The anisotropic formulation also offers practical advantages. Independent control of transverse and axial bin widths enables resolution to be concentrated where interaction effects are expected, without sacrificing statistical precision elsewhere. Monte Carlo simulations confirm that the proposed estimators remain unbiased under both the SFC and SMC global load-sharing models and quantify the finite-sample variability expected in practice. Variability is largest at small separations and under strongly nonuniform axial break intensity, emphasizing that anisotropy is not merely physically appropriate but necessary for resolving localized interaction signatures.

6.2. The Fiber Interaction Statistic

Although the anisotropic PCF completely characterizes second-order spatial structure, it reflects not only mechanically induced interactions but also differences in fiber arrangement and axial break intensity. The fiber interaction statistic Ψ, on the other hand, isolates true interaction effects by normalizing out both the transverse contribution arising from fiber arrangement and the axial contribution associated with the break intensity profile. Under the separable GLS null hypothesis, $\Psi = 1$ at all separations; departures from unity indicate coupling between axial and transverse fracture processes, i.e., local load sharing. Because the normalization is performed against the measured axial intensity profile rather than an assumed form, Ψ applies equally to SFC, SMC, and any other axial break distribution.

Beyond simply detecting departures from GLS, Ψ quantifies both the magnitude and spatial extent of mechanically induced interactions. Because $\mathbb{E}[\Psi] = 1$ under GLS at all separations, deviations above unity provide a direct measure of the interaction strength, while the separations over which Ψ exceeds unity define the interaction range. Local load sharing is therefore expected to manifest as $\Psi > 1$ at small transverse and axial separations, with Ψ approaching unity as separations exceed the characteristic load-transfer length. The transverse distance over which Ψ decays to unity therefore provides a direct estimate of the interaction range, whereas its peak value reflects the intensity of local load sharing.

Ψ also provides a quantitative bridge between experimental fracture datasets and micromechanical models. Forward models predict damage evolution for assumed load-sharing rules, whereas the present framework addresses the complementary inverse problem by determining whether those interaction laws are consistent with experimentally observed fracture patterns. Together, forward simulations and inverse statistical characterization provide a systematic route for calibrating and validating load-sharing models directly against spatially resolved damage data. Because Ψ is resolved in both transverse and axial directions, it provides a substantially more discriminating validation target than composite strength or pullout length distributions alone.

6.3. Variability, Bin Size, and Experimental Design

Finite-sample variability is inherent in spatial statistics of fiber fracture. Both experimental (XCT) and computational (FEA) datasets are limited by specimen dimensions, fiber count, and the number of fracture events. Monte Carlo simulations provide a practical means of quantifying estimator uncertainty and establishing confidence limits. For the SFC model, the standard deviation of Ψ scales approximately with the inverse square root of the number of sampled breaks; similar scaling is observed for the SMC model, although with additional variance arising from axial nonuniformity.

Bin size governs the tradeoff between spatial resolution and statistical precision. Small bins improve resolution but contain relatively few point pairs, increasing estimator variance; larger bins reduce variance but dilute localized signals. The results suggest that transverse bin widths should be selected to match the expected load-transfer length scale. Because this scale is generally unknown, analyses performed over a range of bin sizes provide a practical means of identifying the characteristic interaction distance.

Increasing axial bin width beyond the interaction length scale yields diminishing returns: once fibers are sufficiently sampled, variance is controlled by the number of fibers rather than specimen length. Consequently, increasing the number of sampled fibers—for example, through larger fiber tows or multiple specimens—is generally more effective than increasing gauge length. Finally, datasets exhibiting similar interaction behavior may be compared directly or pooled to improve statistical precision, even when fiber arrangements or axial break distributions differ.

6.4. Limitations

The Monte Carlo simulations presented here employ periodic boundary conditions to eliminate edge effects and isolate the intrinsic finite-sample variability. Application to experimental datasets will require edge-correction procedures to account for missing neighbors near specimen boundaries, particularly at larger separation distances. Simulations of the type presented here would provide a convenient framework for evaluating such correction strategies.

The present formulation also assumes straight, unidirectional fibers. Extension to woven or braided composites is conceptually straightforward but would require redefining the local coordinate system to follow the fiber architecture. Likewise, although the statistical framework itself is independent of the underlying load-sharing mechanism, interpreting the resulting interaction statistics ultimately requires comparison with appropriate micromechanical models.

6.5. Broader Applicability

Although developed for fiber fracture in unidirectional ceramic composites, the methodology applies more generally whenever damage in a heterogeneous material can be represented as a spatial point process and an appropriate mechanics-based null hypothesis can be established. The essential requirement is the ability to distinguish the spatial distribution of potential damage sites and event intensity from mechanically induced interactions.

Potential applications include void nucleation and coalescence during ductile fracture, particle fracture in particulate composites and battery electrodes, microcracking in brittle ceramics and geomaterials, failure localization in architected lattice materials, and damage evolution in polymer matrix composites. In each case, the central question is the same: whether observed clustering reflects genuine mechanical interactions or merely the underlying distribution of potential failure sites.

7. Conclusions

This work establishes a mechanics-based anisotropic spatial statistical framework for interrogating three-dimensional fiber fracture patterns in unidirectional composites. By decomposing pairwise fiber break separations into transverse and axial components, the formulation reflects the directional mechanics of stress redistribution and addresses the inverse problem of distinguishing genuine fiber–fiber interactions from spatial organization arising from fiber arrangement, nonuniform break intensity, or statistical fluctuations alone.

The central theoretical result is that, under global load sharing, the anisotropic pair correlation function is separable in transverse and axial coordinates. This separability provides a rigorous mechanics-based null hypothesis for mechanical independence. A normalized fiber interaction statistic, Ψ, then removes the contributions of fiber arrangement and the observed axial break intensity profile, allowing localized interactions to be isolated regardless of the form of the axial fracture distribution. Monte Carlo simulations demonstrate that the proposed estimators remain unbiased under canonical global load sharing conditions, possess sufficient statistical power to detect short-range correlated fracture over experimentally relevant length scales, and establish how estimator uncertainty scales with specimen size, fiber count, and bin resolution.

More broadly, the framework provides a quantitative bridge between micromechanical models and volumetric experimental observations. Rather than validating load-sharing models solely against macroscopic quantities such as composite strength, it enables direct comparison between predicted and observed spatial damage patterns. Although demonstrated for fiber fracture in unidirectional composites, the methodology is applicable whenever damage can be represented as a spatial point process and a suitable mechanics-based null hypothesis can be formulated. As volumetric imaging techniques continue to mature, such inverse statistical approaches offer a general route for extracting the underlying interaction mechanisms governing heterogeneous material failure from three-dimensional damage data.

AI Use Declaration

During the preparation of this work, the authors used generative AI tools (Anthropic Claude and Open AI Chat GPT) to assist with language editing and manuscript clarity. The authors reviewed and edited the content as needed and take full responsibility for the content of the publication.

CRediT authorship contribution statement

Shane P. Gallagher: Writing – review & editing, Writing – original draft, Software, Methodology, Formal analysis, Conceptualization. **Frank W. Zok:** Writing – review & editing, Supervision, Project administration, Methodology, Funding acquisition, Conceptualization.

Declaration of competing interest

The authors do not have any competing interests.

Acknowledgements

This work was supported by the Pratt & Whitney Center of Excellence in Composites at the University of California, Santa Barbara.

Data availability

No data was used for the research described in the article.

References

Almansour, A., Maillet, E., Ramasamy, S., Morscher, G.N., 2015. Effect of fiber content on single tow SiC minicomposite mechanical and damage properties using acoustic emission. Journal of the European Ceramic Society 35, 3389–3399. https://doi.org/10.1016/j.jeurceramsoc.2015.06.001.
Badran, A., Marshall, D., Legault, Z., Makovetsky, R., Provencher, B., Piché, N., Marsh, M., 2020. Automated segmentation of computed tomography images of fiber-reinforced composites by deep learning. J Mater Sci 55, 16273–16289. https://doi.org/10.1007/s10853-020-05148-7.
Bhattacharyya, R., Adams, D., 2021. Multiscale analysis of multi-directional composite laminates to predict stiffness and strength in the presence of micro-defects. Composites Part C: Open Access 6, 100189. https://doi.org/10.1016/j.jcomc.2021.100189.
Boyer, D., Tarjus, G., Viot, P., Talbot, J., 1995. Percus–Yevick-like integral equation for random sequential addition. J. Chem. Phys. 103, 1607–1613. https://doi.org/10.1063/1.469783.
Callaway, E.B., Zok, F.W., 2020. Tensile response of unidirectional ceramic minicomposites. Journal of the Mechanics and Physics of Solids 138, 103903. https://doi.org/10.1016/j.jmps.2020.103903.
Chateau, C., Gélébart, L., Bornert, M., Crépin, J., 2015. Micromechanical modeling of the elastic behavior of unidirectional CVI SiC/SiC composites. International Journal of Solids and Structures 58, 322–334. https://doi.org/10.1016/j.ijsolstr.2014.11.020.
Cizungu, N.C., Tshibasu, E., Lutete, E., Mushagalusa, C.A., Mugumaarhahama, Y., Ganza, D., Karume, K., Michel, B., Lumbuenamo, R., Bogaert, J., 2021. Fire risk assessment, spatiotemporal clustering and hotspot analysis in the Luki biosphere reserve region, western DR Congo. Trees, Forests and People 5, 100104. https://doi.org/10.1016/j.tfp.2021.100104.
Curtin, W.A., 1991a. Theory of Mechanical Properties of Ceramic-Matrix Composites. Journal of the American Ceramic Society 74, 2837–2845. https://doi.org/10.1111/j.1151-2916.1991.tb06852.x.
Curtin, W.A., 1991b. Exact theory of fibre fragmentation in a single-filament composite. J Mater Sci 26, 5239–5253. https://doi.org/10.1007/BF01143218.
Curtin, W.A., 1993. Fiber pull-out and strain localization in ceramic matrix composites. Journal of the Mechanics and Physics of Solids 41, 35–53. https://doi.org/10.1016/0022-5096(93)90062-K.
da Silva, E.C., Silva, A.C., de Paiva, A.C., Nunes, R.A., Gattass, M., 2008. Diagnosis of solitary lung nodules using the local form of Ripley's *K* function applied to three-dimensional CT data. Computer Methods and Programs in Biomedicine 90, 230–239. https://doi.org/10.1016/j.cmpb.2008.02.003.
Diggle, P., 1983. Statistical analysis of spatial point patterns. Mathematics in biology. Academic Press, London.
Han, N., Christensen, V.L., McAllister, M., Zok, F.W., 2025. Tensile properties of SiC/SiC obtained from epoxy-encapsulated minicomposites. International Journal of Applied Ceramic Technology 22, e14961. https://doi.org/10.1111/ijac.14961.
Han, N., McAllister, M., Gallagher, S.P., Maxwell, P., Zok, F.W., n.d. Spatial autocorrelation of fiber fracture in composites: Experimental studies.
Han, N., Zok, F.W., 2026. Spatial autocorrelation of fiber fracture in ceramic composites: Theory and simulations. Journal of the American Ceramic Society 109, e70403. https://doi.org/10.1111/jace.70403.
Hilmas, A.M., Sevener, K.M., Halloran, J.W., 2020. Damage evolution in SiC/SiC unidirectional composites by X-ray tomography. Journal of the American Ceramic Society 103, 3436–3447. https://doi.org/10.1111/jace.17017.
Hui, C.-Y., Phoenix, S.L., Ibnabdeljalil, M., Smith, R.L., 1995. An exact closed form solution for fragmentation of Weibull fibers in a single filament composite with applications to fiber-reinforced ceramics. Journal of the Mechanics and Physics of Solids 43, 1551–1585. https://doi.org/10.1016/0022-5096(95)00045-K.
Hurtado-Gil, L., Stoica, R.S., Martínez, V.J., Arnalte-Mur, P., 2021. Morphostatistical characterization of the spatial galaxy distribution through Gibbs point processes. Mon Not R Astron Soc 507, 1710–1722. https://doi.org/10.1093/mnras/stab2268.
Ibnabdeljalil, M., Curtin, W.A., 1997. Strength and reliability of fiber-reinforced composites: Localized load-sharing and associated size effects. International Journal of Solids and Structures 34, 2649–2668. https://doi.org/10.1016/S0020-7683(96)00179-5.
Landis, C.M., Beyerlein, I.J., McMeeking, M., 2000. Micromechanical simulation of the failure of fiber reinforced composites. J. Mech. Phys. Solids 48, 621–648. https://doi.org/10.1016/S0022-5096(99)00051-4.
Landis, C.M., McMeeking, R.M., 1999. Stress concentrations in composites with interface sliding, matrix stiffness and uneven fiber spacing using shear lag theory. International Journal of Solids and Structures 36, 4333–4361. https://doi.org/10.1016/S0020-7683(98)00193-0.
Møller, J., Safavimanesh, F., Rasmussen, J.G., 2016. The cylindrical K-function and Poisson line cluster point processes. https://doi.org/10.48550/arXiv.1503.07423.
Morscher, G.N., 1997. Tensile Stress Rupture of SiCf/SiCmMinicomposites with Carbon and Boron Nitride Interphases at Elevated Temperatures in Air. Journal of the American Ceramic Society 80, 2029–2042. https://doi.org/10.1111/j.1151-2916.1997.tb03087.x.
Ripley, B.D., 2005. Spatial Statistics. John Wiley & Sons.
Ripley, B.D., 1977. Modelling Spatial Patterns. Journal of the Royal Statistical Society: Series B (Methodological) 39, 172–192. https://doi.org/10.1111/j.2517-6161.1977.tb01615.x.
Rossoll, A., Moser, B., Mortensen, A., 2012. Tensile strength of axially loaded unidirectional Nextel 610™ reinforced aluminium: A case study in local load sharing between randomly distributed fibres. Composites Part A: Applied Science and Manufacturing 43, 129–137. https://doi.org/10.1016/j.compositesa.2011.09.027.
Safavimanesh, F., Redenbach, C., 2016. A comparison of functional summary statistics to detect anisotropy of three-dimensional point patterns. https://doi.org/10.48550/arXiv.1604.04211.
Sutcu, M., 1989. Weibull statistics applied to fiber failure in ceramic composites and work of fracture. Acta Metallurgica 37, 651–661. https://doi.org/10.1016/0001-6160(89)90249-6.

Swaminathan, B., McCarthy, N.R., Almansour, A.S., Sevener, K., Pollock, T.M., Kiser, J.D., Daly, S., 2021. Microscale characterization of damage accumulation in CMCs. Journal of the European Ceramic Society, Science of High-Temperature Ceramic-matrix Composites 41, 3082–3093. https://doi.org/10.1016/j.jeurceramsoc.2020.05.077.

Swolfs, Y., Morton, H., Scott, A.E., Gorbatikh, L., Reed, P.A.S., Sinclair, I., Spearing, S.M., Verpoest, I., 2015. Synchrotron radiation computed tomography for experimental validation of a tensile strength model for unidirectional fibre-reinforced composites. Composites Part A: Applied Science and Manufacturing 77, 106–113. https://doi.org/10.1016/j.compositesa.2015.06.018.

Terban, M.W., Billinge, S.J.L., 2022. Structural Analysis of Molecular Materials Using the Pair Distribution Function. Chem. Rev. 122, 1208–1272. https://doi.org/10.1021/acs.chemrev.1c00237.

Thouless, M.D., Evans, A.G., 1988. Effects of pull-out on the mechanical properties of ceramic-matrix composites. Acta Metallurgica 36, 517–522. https://doi.org/10.1016/0001-6160(88)90083-1.